

To appear in the Sept. 2001 issue of The Astronomical Journal

## Millimetric Observations of the Center of M81 : A Starved Nucleus with Intraday Variability

Kazushi Sakamoto<sup>1,2</sup>, Hiroyuki Fukuda<sup>3</sup>, Keiichi Wada<sup>3</sup>, and Asao Habe<sup>4</sup>

### ABSTRACT

The central kiloparsec of M81 has been observed in the CO(J=1-0) line and the 3 mm continuum at 100 pc resolution in an attempt to probe molecular gas, and to search for the nuclear inner Lindblad resonance (NILR), around the low-luminosity AGN M81\*. We found the following. (1) Molecular gas in the central kpc is mainly on a “pseudoring” or a spiral arm at a radius of about 500 pc. (2) The region within  $\sim 300$  pc from the nucleus is mostly devoid of molecular gas except for diffuse one; in particular, there is neither a giant molecular cloud that is now accreting on the nucleus nor a conspicuous gas feature that can be identified as an NILR. (3) The 3 mm continuum emission shows significant intraday variation, suggesting an emitting region of  $\sim 100$  AU. (4) The  $3\sigma$  upper limit for CO absorption toward the continuum source is  $\int \tau_{\text{CO}(0\rightarrow 1)} dV < 0.1$  for a linewidth of  $10 \text{ km s}^{-1}$ . The dearth of accreting molecular gas in the vicinity of the nucleus may explain the low luminosity of M81\*.

*Subject headings:* galaxies: active — galaxies: individual (M81, NGC3031) — galaxies: ISM — galaxies: kinematics and dynamics — galaxies: spiral

### 1. Introduction

M81 is a large ( $L_B = 2 \times 10^{10} L_\odot$ ; Tully 1988), early-type (SA(s)ab; de Vaucouleurs *et al.* 1991), spiral galaxy at a distance of 3.6 Mpc (Freedman *et al.* 1994). At the center of M81 is an AGN called M81\*, for which an accreting massive black hole has been indicated by, among other things, a power-law X-ray continuum, a broad H $\alpha$  line, a compact core-jet structure in radio wavelengths, and rapid variability of these features (Ishisaki *et al.* 1996; Bartel & Bietenholz 2000;

---

<sup>1</sup>Nobeyama Radio Observatory, Minamisaku, Nagano, 384-1305, Japan

<sup>2</sup>Harvard-Smithsonian Center for Astrophysics, Submillimeter Array, P. O. Box 824, Hilo, HI 96721, E-mail: ksakamoto@cfa.harvard.edu

<sup>3</sup>National Astronomical Observatory, Mitaka, Tokyo, 181-8588, Japan

<sup>4</sup>Department of Physics, Hokkaido University, Sapporo, 060-0810, Japan

Bower *et al.* 1996, and references therein). In fact, M81 is one of the nearest galaxies that host an AGN with such strong evidence. The luminosity of the nucleus,  $L_{2-10\text{keV}} \sim 2 \times 10^{40}$  erg s<sup>-1</sup>,  $L_{\text{H}\alpha} \sim 4 \times 10^{37}$  erg s<sup>-1</sup>, and  $L_{6\text{cm}} \sim 1 \times 10^{20}$  W Hz<sup>-1</sup> str<sup>-1</sup>, places it among the low-luminosity AGN (Ishisaki *et al.* 1996; Ho, Filippenko, & Sargent 1997; de Bruyn *et al.* 1976).

An interesting issue that can be addressed from observations of molecular gas around M81\* is fueling to the active nucleus; e.g., whether the low-luminosity AGN is suffering from a shortage of fuel. Also related to this issue is the search for the nuclear inner Lindblad resonance (NILR)<sup>5</sup> that is predicted to form around a central massive black hole and help fuel it (Fukuda, Wada, & Habe 1998; Fukuda, Habe, & Wada 2000, hereafter referred to as FWH98 and FHW00, respectively). The proximity of M81 and the estimated mass of the central black hole, ranging from  $(3-8) \times 10^5 M_{\odot}$  to  $> 4 \times 10^7 M_{\odot}$  (Filippenko & Sargent 1988; Iyomoto & Makishima 2001, and references therein) provide a good chance to detect the NILR. Conveniently, M81 has a small nuclear bar of  $\sim 1$  kpc length that could drive the resonance (Elmegreen, Chromey, & Johnson 1995; Reichen *et al.* 1994). In addition, millimeter continuum emission from M81\*, which is strong thanks to the galaxy’s proximity, allows us to probe the tenuous molecular gas in front of the nucleus through absorption studies. Further, monitoring the millimeter continuum during observations tells us the variability of M81\*.

CO emission from cold molecular gas in the center of M81 was first detected by Sage & Westpfahl (1991) using the NRAO 12 m telescope. No further observation has been reported, and, hence, the distribution of molecular gas around the nucleus has not been known to better than 1 kpc resolution. Millimeter continuum emission from M81\* was detected once by Reuter & Lesch (1996) but no monitoring has been reported.

We observed the central kpc (1′) of M81 at  $\sim 100$  pc resolution in CO(J=1–0) line and 3 mm continuum using the Nobeyama Millimeter Array (NMA). The data revealed, for the first time, the distribution of molecular gas in the vicinity of the nucleus, served as a monitor of the continuum emission from M81\* with a time resolution of  $\sim 30$  min, and also allowed us to search for cold molecular gas in front of the nucleus through absorption.

## 2. Observations and Data Reduction

We observed the CO(J=1–0) line and 3 mm continuum using the NMA from November 1999 to January 2000 and in April 2000. The six 10 m telescopes of the array are equipped with SIS receivers of single polarization and have 1′ beamsizes in FWHM. They were pointed toward M81\* at  $\alpha_{\text{B1950}} = 9^{\text{h}}51^{\text{m}}27^{\text{s}}.3004$  and  $\delta_{\text{B1950}} = +69^{\circ}18'08''.267$  (Ma *et al.* 1998). The log of observations is

---

<sup>5</sup>The name of the resonance was “nuclear Lindblad resonance (NLR)” when it was first proposed. However, we rename it in this paper to avoid confusion with the “narrow line region” whose widely-used acronym in AGN studies is also NLR. The new name also makes it clear that the resonance is an inner Lindblad resonance (see §4).

in Table 1. We obtained seven transits in the most compact D configuration and one in the sparse AB configuration. Two sets of correlators, UWBC and FX, were used simultaneously, with UWBC covering 512 MHz ( $1300 \text{ km s}^{-1}$  for CO) with 256 channels and FX covering 32 MHz ( $80 \text{ km s}^{-1}$  for CO) with 1024 channels. This setup was used to observe the broad CO emission line ( $\Delta V \sim 400 \text{ km s}^{-1}$ ) and to search for a narrow absorption line of CO against the continuum emission from M81\*. The CO line was observed in the upper sideband (USB) at 115 GHz, while continuum data were obtained from the lower sideband (LSB) at 103 GHz, where the atmospheric attenuation is less severe. Data from both sidebands were recorded in every 8 sec; this high rate was employed to reduce coherence loss in the measurements of continuum flux density. In each transit, M81 and a quasar B0836+710, which is  $6^\circ$  away from M81, were observed in 20- or 30-min cycles, and either 3C273 or 3C279 was observed for  $\sim 30$  min for passband calibration. Atmospheric attenuation was corrected by the chopper-wheel method. Flux scale was established by comparing quasars with Uranus. The flux density of the calibrator B0836+710 was measured a total of 14 times during our observations. It was 1.4 Jy in the first session of observations from November through January and 1.6 Jy in the second session in April, being constant during each session, with about  $\pm 10\%$  error.

Maps of CO emission were made using standard data-reduction techniques for radio interferometry, including gain and passband calibration as well as continuum subtraction in UVPROC2, and Fourier transform and deconvolution in AIPS. Data from the AB configuration were not used to make maps of CO emission, because little emission was detected in long baselines. Resulting CO maps have a resolution of  $6''.9 \times 5''.8$  (P.A. =  $-36^\circ$ ), which corresponds to  $120 \times 100$  pc at the distance of the galaxy. The maps in this paper are not corrected for the primary beam response, but all flux measurements have been corrected for it.

Absorption of CO has been searched in both UWBC and FX data. UWBC data were binned every 2 channels to obtain 4 MHz ( $10.4 \text{ km s}^{-1}$ ) resolution, while FX data were binned every 16 channels to obtain 0.5 MHz ( $1.3 \text{ km s}^{-1}$ ) resolution. Flux density of the nucleus was measured in each channel of the data cubes that were made without continuum subtraction, and provided spectra of the central 100 pc of M81. Linear baseline was subtracted from each spectrum, to cancel small differences in spectral index between M81\* and the passband calibrators. The rms of each spectrum is 0.032 and 0.14 for UWBC and FX spectrum, respectively, in the unit where the flux density of M81\* is unity.

Variations in M81\* were monitored using the LSB data. The LSB data were first averaged over the 512 MHz band, and then averaged over the 20- or 30-min of time between gain calibrator observations. The latter averaging was made for visibility amplitudes to avoid coherence loss. Arithmetic averaging of amplitudes (so-called ‘scalar averaging’) was used when the signal-to-noise ratio of each visibility was high enough ( $> 7$ ), and the maximum likelihood method was used when it was not, thus avoiding bias due to amplitude averaging. The LSB data for 0836+710 were reduced in the same way, and used to remove any variation in system and atmospheric conditions. The use of 0836+710 as a gain calibrator here, as well as in the mapping above, has a built-in assumption that it had a constant flux density and was unpolarized during each transit. We believe the assumption

is found as discussed below.

### 3. Results

#### 3.1. CO emission

Figures 1 and 2 show CO channel maps and the integrated intensity map, respectively. The CO emission is greater than  $3\sigma$  from  $-187 \text{ km s}^{-1}$  to  $146 \text{ km s}^{-1}$ , with nondetection in two channels near the systemic velocity. The velocity range, as well as the depression near the systemic velocity, is in good agreement with the previous single-dish observations. It is evident in the maps that CO emission is seen *around* the galactic center, mostly at galactocentric radii of between 300 and 600 pc. The gas distribution is lopsided, and little emission is seen to the west of the nucleus. For simplicity, we call the overall structure a “pseudoring” at a galactocentric distance of about 500 pc, though our data do not rule out other descriptions for the structure, such as spiral arm(s). In fact, a somewhat similar structure in H $\alpha$  was called “nuclear spiral” in Devereux *et al.* (1995). The pseudoring has a peak molecular gas surface density  $120 M_{\odot} \text{ pc}^{-2}$  at our resolution, where no correction for inclination has been made, and the following Galactic CO-to-H $_2$  conversion relation is assumed (Scoville *et al.* 1987; Solomon *et al.* 1987; Strong *et al.* 1988):

$$\left( \frac{\Sigma_{\text{mol}}}{M_{\odot} \text{ pc}^{-2}} \right) = 6.8 \times 10^2 \left( \frac{I_{\text{CO}}}{\text{Jy km s}^{-1} \text{ arcsec}^{-2}} \right). \quad (1)$$

The total mass of molecular gas in the pseudoring is  $1 \times 10^7 M_{\odot}$ , and the structure is apparently made of several gas clumps. The peak brightness temperature of each clump is  $\sim 0.3 \text{ K}$  when averaged over our beam size of  $\sim 100 \text{ pc}$  and a velocity width of  $21 \text{ km s}^{-1}$ , comparable to those for giant molecular clouds (GMCs) and GMC complexes in the outer regions of M81 (Taylor & Wilson 1998; Brouillet *et al.* 1998). It is also notable that the nucleus is devoid of CO emission. The closest components to the nucleus are the GMCs seen in the  $-124, -104,$  and  $+42 \text{ km s}^{-1}$  maps at the deprojected galactocentric radius of  $\sim 300 \text{ pc}$ . Their masses are  $M_{\text{mol}} \sim 5 \times 10^5 M_{\odot}$ .

Figure 3 is the CO spectrum observed with NMA, whose primary beam is  $60''$  in FWHM. The total CO flux is  $50 \text{ Jy km s}^{-1}$ , which is half the single-dish flux observed with the NRAO 12 m telescope in its  $55''$  beam (Sage & Westpfahl 1991). Thus, provided that calibrations are accurate in both observations, we recovered about half the total CO flux; the rest must be either too extended or too faint (or both) to be detected with our interferometric observations. If the missed emission is uniformly distributed in our field of view and has a linewidth of  $20 \text{ km s}^{-1}$  or smaller at each position, then its intensity in our channel maps would be  $28 \text{ mJy beam}^{-1}$ , while the rms in the channel maps is  $13 \text{ mJy beam}^{-1}$ . It thus seems more likely that the missing flux is mainly due to a smoothly distributed population of small molecular clouds in the central kiloparsec. Widespread distribution of small clouds, in addition to larger GMCs, has been suggested also on a spiral arm of M81 (Brouillet *et al.* 1998).

The overall rotation seen in the channel maps is largely consistent with what is expected from the moderately inclined ( $i = 58^\circ$ ) galaxy whose receding major axis is at P.A. =  $330^\circ$  (Adler & Westpfahl 1996). Detailed velocity field structure is hard to discern in the limited spatial coverage of the current data, but obvious noncircular motions are not seen. The CO linewidth of  $\sim 350$  km s $^{-1}$  is already attained at a radius of  $\sim 30''$ , while the linewidth of HI peaks at about 420 km s $^{-1}$  at a radius of  $\sim 400''$  (Adler & Westpfahl 1996). If the inner CO and outer HI disks are coplanar and neither of them is affected by noncircular motions, then the rotation curve of M81 reaches 80% of its maximum already at a radius of 500 pc. If the above assumptions hold, then the rotation curve is steeper in the central regions than estimated from previous HI observations (Fig. 7 of Adler & Westpfahl 1996), but is consistent with ones observed in spiral galaxies of similar luminosity (Sakamoto *et al.* 1999a). This is not surprising considering the lower spatial resolution of the HI observations. The Keplerian dynamical mass calculated from the CO linewidth is  $M_{\text{dyn}}(r \leq 500 \text{ pc}) = 1 \times 10^{10} M_\odot$ .

The active nucleus M81\* appears to be very close to the dynamical center of the galaxy; a conservative upper limit to the offset is  $10''$  or 200 pc. Thus M81\* is not significantly displaced from the dynamical center despite its small mass, which Ho, Filippenko, & Sargent (1996) estimated to be  $0.7 - 3 \times 10^6 M_\odot$  comparable to that of a GMC complex.

### 3.2. Continuum emission

Continuum emission is detected only from the nucleus, and its flux density varied during our observations. Figure 4 shows amplitudes of M81\* and 0836+710 during observations on 2000 January 1 and 3. The upper panels show data before the gain calibration using 0836+710 but after the chopper-wheel calibration. The data taken in better weather on January 1 show that the amplitude of 0836+710 was constant to  $\lesssim 5\%$  during the 6-hr observations, in which the parallactic angle of the source changed almost linearly by  $\sim 100^\circ$ . The amplitude should have varied sinusoidally if the source was linearly polarized, because we observed in linear polarization mode with position angle rotating with the parallactic angle. The constant amplitude suggests that 0836+710 had a constant flux density and a negligible degree of linear polarization, unless 0836+710 varied to compensate for polarization, which is unlikely. We also did not see significant variation in the amplitude of 0836+710 during observations made on other dates in stable weather conditions.

The lower panels in Fig. 4 show data after gain calibration, in which a gain curve is obtained by interpolating the amplitude of 0836+710 with a Gaussian kernel that has  $\sigma = 0.015$  day and a cutoff at  $\Delta t = 0.050$  day. The gain calibration is necessary and useful, especially for data taken in changing weather conditions, such as those on January 3. The common variation seen in the two sources on that date must be mostly due to varying radio seeing and coherence loss, judging from the correlation between the amplitudes and the scatter in visibility phases. After the gain calibration, the amplitude of M81\* shows almost linear variation on both dates. The lack of a sinusoidal pattern suggests that the linear polarization of M81\* is not large enough to dominate

the amplitude variation, and that the amplitude variation is mainly due to the variation of the total flux density of M81\*.

Table 2 lists the flux density of M81\* and its rate of variation for each night. The most important result is that M81\* varies in almost every track of duration 5–10 hrs by a few to several 10 %. In particular, M81\* appears to have had a flare on J.D.= 2451456, as shown in Fig. 5. During our observing period of 152 days, the ratio of the maximum to the minimum flux density is  $\sim 7$ , and the mean flux density is 0.39 Jy, a factor of 2 larger than the only previous measurement (at 3.4 mm) made in 1993 by Reuter & Lesch (1996). It is also notable that variability is almost linear in each day and that we do not see significant variation with timescales of a few hours or less, even though the resolution of our observations is  $\sim 0.5$  hrs.

To characterize the timescale of the variation, doubling time is calculated as the time in which M81\* would have varied by a factor of 2 if it had held its linear trend in variation in each track. We do this extrapolation because M81\* did not show two-fold variation in any single track. The largest variation seen in a single track is the 45% increase during the 0.24-day observations on January 1. The doubling timescales defined this way are  $\sim 1$  day, as listed in Table 2. Also, flux density (without extrapolation) doubled in 1.2 days during our first 2 days of observations. Thus M81\* has intraday variability at 3 mm.

The variation of radio emission from M81\* has long been known in centimeter wavelengths (Crane *et al.* 1976; de Bruyn *et al.* 1976; Ho *et al.* 1999; Bietenholz *et al.* 2000), with the degree of variation being about a factor of 2 over years and being smaller in longer wavelengths. Although 40% variation in 4 days was observed in 1974 by Crane *et al.* (1976), recent extensive observations did not agree on the variation in short timescales ( $\sim$  days). While Ho *et al.* (1999) reported 10–60 % variation on the timescale of  $\lesssim 1$  day at 3.6 cm, Bietenholz *et al.* (2000) did not see variations larger than their 5% standard error in their 12 epochs of 12–18 hr observations at the same wavelength. Our observations show that intraday variability does exist at a millimeter wavelength. The larger degree of variation (a factor of 7 in our observing period of 5 months) is in accordance with the trend that the degree of variation increases with frequency.

The sizescale of the millimeter-emitting region should be below about 1 light-day or a few 100 AU from the light-crossing time argument, if there is no relativistic beaming. This size is consistent with what is extrapolated from VLBI observations in centimeter wavelengths, where the size is 700 AU in 22 GHz and changes with frequency as  $\nu^{-0.8}$  between 2.3 and 22 GHz (Bietenholz *et al.* 1996). It is also comparable to the size of the broad-line region in this galaxy (Filippenko & Sargent 1988; Ho, Filippenko, & Sargent 1996). For a source 1 light-day or smaller, the brightness temperature needs to be greater than  $10^{11}$  K at 3 mm in order to have a flux density of 1 Jy. The 3 mm emission from M81\* is obviously nonthermal, as is the case with the centimeter emission, and the high brightness temperature is comparable to those observed in the cores of radio galaxies.

### 3.3. CO absorption

Figure 6 shows spectra of M81\*, at high- and low-velocity resolutions, in the frequencies where CO(0→1) absorption would be caused by molecular gas in either M81 or the Galaxy or both. No absorption is seen in the spectra. The  $3\sigma$  upper limit of the CO optical depth is 0.1 and 0.5 for linewidths of  $10.4 \text{ km s}^{-1}$  and  $1.3 \text{ km s}^{-1}$ , respectively.

Hydrogen column density toward M81\* has been estimated from X-ray observations to be  $N_{\text{H}} \sim 1 \times 10^{21} \text{ cm}^{-2}$  (Ishisaki *et al.* 1996; Pellegrini *et al.* 2000). If the absorbing material is mostly molecular gas with a CO abundance of  $[\text{CO}]/[\text{H}_2] = 10^{-4}$ , then the integrated optical depth of CO,  $\int \tau_{\text{CO}(0 \rightarrow 1)} dV$ , would be 10 and  $1 \text{ km s}^{-1}$  for LTE temperatures of 10 and 30 K, respectively. The CO absorption should have been detected in the case of lower temperature gas. Possible reasons for the nondetection therefore include ionized or atomic absorbing material, low CO abundance, high temperature ( $> 30 \text{ K}$ ) of molecular gas, and a large velocity width of the absorbing gas.

## 4. Search for the Nuclear Inner Lindblad Resonance

Nuclear inner Lindblad resonance is the resonance between perturbations from a stellar bar and epicyclic motion of gas clouds orbiting around the galactic center that hosts a central massive black hole (FWH98). It is formed, like other inner Lindblad resonances, on the radius at which  $\Omega - \kappa/2$  is equal to  $\Omega_{\text{bar}}$ , where  $\Omega$  is angular frequency of the orbiting clouds,  $\kappa$  is the epicyclic frequency, and  $\Omega_{\text{bar}}$  is the pattern speed of the bar. Figure 7 shows a model rotation curve and its  $\Omega - \kappa/2$  in a potential with a central massive black hole. It is the upturn of the rotation curve toward the central black hole that causes the upturn of the  $\Omega - \kappa/2$  curve and makes the NILR possible. As seen below, *the dynamical effect of a central massive black hole is far-reaching*, being able to form the NILR even at a radius within which only  $\sim 1 \%$  of the total mass is due to the black hole.

### 4.1. Maximum Radius of NILR

The maximum radius at which an NILR can be formed is where  $\Omega - \kappa/2$  is its minimum<sup>6</sup>. This radius,  $\max(R_{\text{NILR}})$ , is expected to be closely related to the radius where the rotation curve hits its minimum. We call the latter radius nuclear turnover and denote it as  $R_{\text{nt}}$ . The nuclear turnover,  $R_{\text{nt}}$ , is observable and can be easily understood as the radius where the mass of the central black hole is comparable to the mass of the other components inside it. For these reasons,  $R_{\text{nt}}$  must be a good scale to measure  $\max(R_{\text{NILR}})$ . In fact, there are cases where the ratio of the two radii,

---

<sup>6</sup>This is also the minimum radius at which the inner inner Lindblad resonance (IILR) can form. The two resonances can degenerate at this radius.

$\max(R_{\text{NILR}})/R_{\text{nt}}$ , can be related to the relative mass of the central black hole with respect to the characteristic mass within the ordinary turnover radius of the rotation curve.

The rotation curve of a galaxy with a central massive black hole can be written, when normalized, in the form

$$v_{\text{total}}(r) = \sqrt{v_g^2(r) + \frac{m}{r}}, \quad (2)$$

where  $r$  and  $v$  are normalized radius and velocity, respectively,  $v_g(r)$  is the normalized rotation curve of the galaxy without the central black hole, and  $m$  is the normalized mass of the black hole. It is assumed that the galaxy is not strongly barred. We normalize radius so that the turnover radius of the rotation curve  $v_g(r)$  is at  $r \simeq 1$  and normalize the velocity so that the flat (or peak) rotation velocity is  $v \simeq 1$ . Consequently, the parameter  $m$  is roughly the ratio of the black hole mass to the galaxy mass within the turnover radius and should satisfy  $m \ll 1$  for most disk galaxies.

Let us consider the case where the rotation curve without the central black hole can be well approximated, from the center through the turnover radius, with the first few terms of the Taylor-expansion,

$$v_g(r) = ar + br^2 + cr^3 + \dots \quad (3)$$

The coefficient  $a$  is positive and of the order of unity, and the first non-zero coefficient after  $a$  is negative and is also of the order of unity. An example of this class is the rotation curve of the logarithmic potential,

$$v_{g,\log}(r) = \frac{r}{\sqrt{1+r^2}} \quad (4)$$

$$= r - \frac{1}{2}r^3 + \dots, \quad (5)$$

where  $a = 1$ ,  $b = 0$ , and  $c = -1/2$ . The radius of nuclear turnover is, for small  $m$ ,

$$r_{\text{nt}} \approx \left(\frac{m}{2a^2}\right)^{1/3}. \quad (6)$$

The maximum radius of the nuclear inner Lindblad resonance is, from the minimum of the  $\Omega - \kappa/2$  curve,

$$\max(r_{\text{NILR}}) \approx \left(-\frac{9m}{2ab}\right)^{1/4} \quad (7)$$

if  $b$  is not zero. It is

$$\max(r_{\text{NILR}}) \approx \left(-\frac{9m}{8ac}\right)^{1/5} \quad (8)$$

if  $b$  is zero but  $c$  is not. The ratio of the two radii is, therefore,

$$\frac{\max(r_{\text{NILR}})}{r_{\text{nt}}} \approx \begin{cases} 1.8 m^{-1/12} a^{5/12} (-b)^{-1/4} & \text{if } b \neq 0 \\ 1.3 m^{-2/15} a^{7/15} (-c)^{-1/5} & \text{if } b = 0 \text{ and } c \neq 0. \end{cases} \quad (9)$$



Ignoring the coefficients  $a, b, c$ , which are of the order of unity, the ratio is in the range of 2–8 for the fractional mass range of  $m = 10^{-2} - 10^{-6}$ . The weak dependence of  $\max(r_{\text{NILR}})$  on the black hole mass  $m$  is notable, and the nearly constant value of the  $\max(r_{\text{NILR}})/r_{\text{nt}}$  for the most realistic range of  $m$  ensures that  $r_K$  can be conveniently used to measure the radius of the NILR.

There are rotation curves for which Taylor expansion is not possible around  $r = 0$  and therefore the above analysis does not apply. However, some of those rotation curves do have similar characteristics on NILR as in the cases discussed above. An example is the rotation curve of an exponential disk with surface density  $\Sigma(R) = \Sigma_0 \exp(R/R_d)$ ,

$$v_{g,\text{exp}}(r) = 2^{3/2} r [I_0(r)K_0(r) - I_1(r)K_1(r)]^{1/2}, \quad (10)$$

where the radius is normalized as  $r \equiv R/2R_d$ , and  $I$  and  $K$  are modified Bessel functions (see Binney & Tremaine (1987) p.77). The turnover radius of the rotation curve is  $r \approx 1.1$ . The conditions that approximately describe  $r_{\text{nt}}$  and  $\max(r_{\text{NILR}})$  are, for small  $m$ ,

$$r_{\text{nt, exp}}^3 (-\log r_{\text{nt, exp}}) \approx \frac{m}{16} \quad (11)$$

and

$$[\max(r_{\text{NILR, exp}})]^3 (-\log r_{\text{NILR, exp}})^{-1} \approx \frac{9m}{4}, \quad (12)$$

respectively. They lead to the formula

$$\frac{\max(r_{\text{NILR, exp}})}{r_{\text{nt, exp}}} \approx \{36 \log [\max(r_{\text{NILR, exp}})] \log r_{\text{nt, exp}}\}^{1/3} \quad (13)$$

that shows the ratio being larger for smaller  $m$  but being very weakly dependent on  $m$ , as is the case for eq. (9). Numerically, the ratio is in the range of 5–9 for  $m = 10^{-2} - 10^{-6}$ .

The parameter  $m$  for M81 is estimated to be  $m \sim 5 \times 10^{-5} - 5 \times 10^{-3}$ , by use of  $M_{\text{dyn}}(r \leq 500 \text{ pc}) = 1 \times 10^{10} M_{\odot}$  obtained from our CO observations and the black hole mass in the literature (see §1). For this range of  $m$ , as we have seen, NILR can be formed at up to several times larger radius than the nuclear turnover. The nuclear turnover radius,  $R_{\text{nt}}$ , can be constrained as  $R_{\text{nt}} \leq 15 - 70 \text{ pc}$  by using the assumption that the mass density is uniform in the central kpc. It is an upper limit because the density most likely increases toward the galactic center, as readily inferred from light distribution. Combining these numbers, we can estimate  $\max(R_{\text{NILR}})$  to be 100 pc for a smaller number for the black hole mass and 300 pc for a larger number. Thus it is unlikely that the gas feature (pseudoring) at around 500 pc is due to an NILR. Note that the radius of an NILR can be much smaller than the upper limits (and  $R_{\text{nt}}$ ) for a large  $\Omega_{\text{bar}}$ .

## 4.2. Numerical Simulations

We made numerical simulations for gas around an NILR by using parameters adjusted for M81 in order to tell what can be seen if there is an NILR in the galaxy. The simulation is non-selfgravitating, isothermal, and two-dimensional. Evolution of a rotating gas disk is simulated in a

time-independent, external potential having a bar and a central black hole. The potential is in the form

$$\Phi_{\text{ext}} \equiv \Phi_{\text{BH}} + \Phi_{\text{bar}} + \Phi_{\text{disk}}, \quad (14)$$

where  $\Phi_{\text{BH}}$ ,  $\Phi_{\text{bar}}$ , and  $\Phi_{\text{disk}}$  are a central massive black hole, a stellar bar, and a disk, respectively. They are defined as follows:

$$\Phi_{\text{BH}}(R) \equiv -\frac{GM_{\text{BH}}}{(R^2 + a^2)^{1/2}}, \quad (15)$$

$$\Phi_{\text{disk}}(R) \equiv -\frac{3^{3/2}}{2} \frac{a_d v_0^2}{(R^2 + a_d^2)^{1/2}}, \quad (16)$$

and

$$\Phi_{\text{bar}}(R, \phi) \equiv -\frac{3^{3/2}}{2} \frac{a_b v_0^2}{(R^2 + a_b^2)^{1/2}} \left[ 1 + \varepsilon_0 \frac{a_b R^2}{(R^2 + a_b^2)^{3/2}} \cos 2\phi \right], \quad (17)$$

with  $a = 10$  pc,  $a_d = 5$  kpc,  $a_b = 0.5$  kpc,  $v_0 = 200$  km s<sup>-1</sup>, and  $\varepsilon_0 = 0.05$ . This model is based on the potentials used in Wada, Minezaki, & Sakamoto (1998). Figure 7 shows the rotation curve and  $\Omega - \kappa/2$  of the model potential with  $M_{\text{BH}} = 10^7 M_\odot$ . The initial gas disk is axisymmetric and rotationally supported, with a uniform surface density and total mass of  $10^7 M_\odot$  within a 2 kpc diameter. The isothermal equation of state is adopted along with a sound velocity of 10 km s<sup>-1</sup>.

We use the second-order Euler mesh code, which is based on the Advection Upstream Splitting Method (AUSM; Liou & Steffen 1993), to solve the hydrodynamical equations. Details of the numerical scheme are described in Wada & Norman (2001). Simulations are made on  $512 \times 512$  Cartesian grid points in a region of  $2 \times 2$  kpc; the spatial resolution is 3.9 pc.

Figure 8 shows time evolution of gas for  $\Omega_{\text{bar}} = 50$  km s<sup>-1</sup> kpc<sup>-1</sup> and  $M_{\text{BH}} = 10^6, 10^7$ , and  $10^8 M_\odot$ . Table 3 lists  $R_{\text{nt}}$ ,  $R_{\text{NILR}}$ , and  $\max(R_{\text{NILR}})$  for each mass of the black hole. The small concentration of gas that develops near the galactic center at  $R \sim R_{\text{NILR}}$  is due to the NILR. The two-armed spiral structure is more clearly seen in cases with larger  $M_{\text{BH}}$ . Evolution of gas around an NILR, especially when the self-gravity of gas is important, has been studied in more detail in FHW00 and in FWH98. Outside NILR, the inner inner Lindblad resonance (IILR) creates an oval-shaped gas distribution, two leading spirals, with its major axis leading the bar major axis by about 45°.

### 4.3. Comparison with Observations

The lack of CO emission around the nucleus, inside the 500 pc pseudoring, prevents us from detecting the features of an NILR. Among the reasons that can possibly explain the absence of these features are the following: 1) the NILR had quickly driven most of gas around the nucleus to the AGN as suggested in FWH00; 2) the gas around the NILR is not in molecular form; 3) the NILR is at a too small radius for us to detect the gas accumulated around the resonance; and 4) the NILR does not exist because of a slow pattern speed or weakness of the bar perturbation. Despite

the nondetection in CO, HST images in optical revealed a spiral dust lane extending  $\sim 12''$  (200 pc) to the north of the nucleus, and a disk-like feature of  $\sim 7''$  (120 pc) diameter in H $\alpha$  (Devereux, Ford, & Jacoby 1997; Pogge *et al.* 2000). These features could be related to an NILR. Kinematical information is needed to confirm the possibility.

The pseudoring (or spiral feature) in molecular gas at  $R \sim 500$  pc is suggestive of a gas dynamical mechanism to arrange gas clouds — possibly an inner Lindblad resonance. The current data, however, are too scarce to pinpoint the mechanism, other than to say that it is unlikely to be an NILR. The dynamics in the central kiloparsec may well be affected by the nuclear bar, or oval distortion, seen in the near-infrared, whose semi-major axis is  $\sim 30''$  (0.5 kpc) at P.A. =  $142^\circ$  (Elmegreen, Chromey, & Johnson 1995). The observed gas distribution, however, does not show twin peaks and/or gas ridges at the bar’s leading side unlike many barred galaxies. The nuclear bar may have too small a quadrupole moment to create those features or may have a deviation from bisymmetry, which causes the lopsided gas distribution.

## 5. Starved Nucleus

M81 does not have much molecular gas in the galactic center. The gas mass in the central kiloparsec is  $\sim 2 \times 10^7 M_\odot$ , which is more than an order of magnitude smaller than the number in more gas-rich spiral galaxies (Sakamoto *et al.* 1999a,b). The mass fraction of molecular gas in the central kiloparsec is  $M_{\text{mol}}/M_{\text{dyn}}(r \leq 500 \text{ pc}) \approx 2 \times 10^{-3}$ , where missing flux is taken into account. The low fraction is in accordance with the trend that galactic nuclei with an optical spectrum indicative of an AGN tend to have a lower gas mass fraction than do galactic nuclei with an HII type spectrum (Sakamoto *et al.* 1999b). The  $3\sigma$  upper limit for the mass of molecular gas in the central 100 pc is  $M_{\text{mol}}^{\text{nuc}} \leq 4 \times 10^5 (\Delta V/100 \text{ km s}^{-1})^{1/2} M_\odot$ , where  $\Delta V$  is the CO linewidth. Thus, it appears that M81\* is starving for infalling interstellar medium.

The lack of significant CO absorption toward M81\* is consistent with its type 1 nature in the framework of the unified scheme, in the sense that the putative accretion disk or broad line region does not suffer much obscuration from surrounding material. On the other hand, the lack of CO emission at the nucleus prevented us from verifying if there is a gas torus or disk around M81\*.

With the paucity of fueling molecular gas around the active nucleus, its activity may well be limited by the intermittent supply of fuel. If the AGN flares up when, for example, the closest GMC starts to interact with the nucleus, the timescale of the variability would depend on the interval between such interactions. If a bar-streaming mechanism that radially transports the nearest GMC complexes to the nucleus is at work, as was observed in NGC 5005 (Sakamoto, Baker, & Scoville 2000), then the timescale would be of the order of Myr ( $\approx 100 \text{ pc}/100 \text{ km s}^{-1}$ ). On the other hand, if dynamical friction to the GMCs is the only mechanism that transports the clouds, then M81\* is really starving and will not get the next large supply of fuel for  $10^9\text{--}10^{10}$  yrs.

Finally, we note that a  $5 \times 10^5 M_\odot$  black hole, like GMCs of similar mass, takes  $10^9\text{--}10^{10}$  yrs

to fall from  $R \sim 300$  pc to the dynamical center through dynamical friction. Thus, if the mass of M81\* is close to the lower value in the literature, M81\* should be older than 1 Gyr or was formed at the very center of the galactic potential or both. Tighter constraints from further observation of this nearby AGN would be useful in studies of the formation and evolution of AGNs.

## 6. Summary

The central kiloparsec of the nearby spiral galaxy M81 has been observed in CO(J=1-0) and, at the same time, its low-luminosity AGN M81\* has been monitored in the 3 mm continuum. A search for NILR has also been carried out for M81. Our observations and analysis yield the following results:

1. Most of the molecular gas in the central kiloparsec is detected on a “pseudoring” or a nuclear spiral at the galactocentric radius of  $\sim 500$  pc. The area within 300 pc from M81\*, which appears to be at the dynamical center, is devoid of CO emission, except for diffuse emission, which can not be detected with our observations. In particular, no CO emission is detected at the nucleus nor is any CO absorption detected against the continuum emission from M81\*. The upper limit for the gas mass in the central 100 pc is  $M_{\text{mol}}^{\text{nuc}} \leq 4 \times 10^5 (\Delta V / 100 \text{ km s}^{-1})^{1/2} M_{\odot}$ . The GMCs nearest to the nucleus are 300 pc away, hence the nucleus will not be fueled by them at least in the next Myr.
2. The 3 mm continuum from M81\* showed conspicuous variation; a factor of 7 in 5 months and up to 45% in 6 hrs. The intraday variation suggests  $\lesssim 100$  AU size and  $\sim 10^{11}$  K brightness temperature for the emitting region.
3. It is pointed out that the maximum radius of the NILR can be several times larger than the radius at which the rotation curve turns over from Keplerian to rigid-body rotation. Despite this factor, the pseudoring at  $R \sim 500$  pc is too far from the nucleus to be due to the NILR. No CO feature that can be associated with an NILR is found in M81.

We are grateful to NRO staff for their help during observations. The NASA Extragalactic Database was used to carry out our research.

## REFERENCES

- Adler, D. S., and Westpfahl, D. J. 1996, *AJ*, 111, 735
- Bartel, N., and Bietenholz, M. 2000, in “Astrophysical Phenomena Revealed by Space VLBI”, Eds., H. Hirabayashi, P. G. Edwards, and D. W. Murphy, (Sagamihara: ISAS), p17
- Bietenholz, M. F. *et al.* 1996, *ApJ*, 457, 604
- Bietenholz, M. F., Bartel, N., Rupen, M.P. 2000, *ApJ*, 532, 895
- Binney, J., and Tremaine, S. 1987, “Galactic Dynamics”, (Princeton: Princeton University Press)
- Bower, G. A., Wilson, A. S., Heckman, T. M., and Richstone, D. O. 1996, *AJ*, 111, 1901
- Brouillet, N., Kaufmann, M., Combes, F., Baudry, A., and Bash, F. 1998, *A&A*, 333, 92
- Crane, P. C., Giuffrida, T. S., and Carlson, J. B. 1976, *ApJ*, 203, L113
- de Bruyn, A. G., Crane, P. C., Price, R. M., and Carlson, J. B. 1976, *A&A*, 46, 243
- de Vaucouleurs, G., de Vaucouleurs, A., Corwin, H. G., Buta, R. J., Paturel, G., & Fouque, P. 1991, “Third Reference Catalogue of Bright Galaxies”, (New York: Springer Verlag)
- Devereux, N. A., Jacoby, G., Ciardullo, R. 1995, *AJ*, 110, 1115
- Devereux, N., Ford, H., and Jacoby, G. 1997, *ApJ*, 481, L71
- Elmegreen, D. M., Chromey, F. R., and Johnson, C. O. 1995, *AJ*, 110, 2102
- Filippenko, A. V., and Sargent, W. L. W. 1988, *ApJ*, 324, 134
- Freedman, W. L. *et al.* 1994, *ApJ*, 427, 628
- Fukuda, H., Wada, K, and Habe, A. 1998 (FWH98), *MNRAS*, 295, 463
- Fukuda, H., Habe, A., and Wada, K. 2000 (FHW00), *ApJ*, 529, 109
- Ho, L. C., Filippenko, A. V., and Sargent, W. L. W. 1996, *ApJ*, 462, 183
- Ho, L. C., Filippenko, A. V., & Sargent, W. L. W. 1997, *ApJS*, 112, 315
- Ho, L. C., van Dyk S. D., Pooley, G. G., Sramek, R. A., and Weiler, K. W. 1999, *ApJ*, 118, 843
- Ishisaki, Y. *et al.* 1996, *PASJ*, 48, 237
- Iyomoto, N., Makishima, K. 2001, *MNRAS*, 321, 767
- Liou, M., Steffen, C. 1993, *J. Comp. Phys.*, 107, 23

- Ma, C. *et al.* 1998, *AJ*, 116, 516
- Pellegrini, S., Cappi, M., Bassani, L., Malaguti, G., Palumbo, G. G. C., and Persic, M. 2000, *A&A*, 353, 447
- Pogge, R. W., Maoz, D., Ho, L. C., and Eracleous, M. 2000, *ApJ*, 532, 323
- Reichen, M., Kaufman, M., Blecha, A., Golay, M., and Huguenin, D. 1994, *A&AS*, 106, 523
- Reuter, H. -P., and Lesch, H. 1996, *A&A*, 310, L5
- Sage, L. J., and Westpfahl, D. J. 1991, *A&A*, 242, 371
- Sakamoto, K., Okumura, S. K., Ishizuki, S., and Scoville, N. Z. 1999a, *ApJS*, 124, 403
- Sakamoto, K., Okumura, S. K., Ishizuki, S., and Scoville, N. Z. 1999b, *ApJ*, 525, 691
- Sakamoto, K., Baker, A. J., and Scoville, N. Z. 2000, *ApJ*, 533, 149
- Scoville, N. Z., Yun, M. S., Clements, D. P., Sanders, D. B., & Walker, W. H. 1987, *ApJS*, 63, 821
- Solomon, P. M., Rivilo, A. R., Barrett, J., & Yahil, A. 1987, *ApJ*, 319, 730
- Strong, A. W. *et al.* 1988, *A&A*, 207, 1
- Taylor, C. L., and Wilson, C. D. 1998, *ApJ*, 494, 581
- Tully, R. B. 1988, “Nearby Galaxies Catalog”, (Cambridge: Cambridge University Press)
- Wada, K., Minezaki, T., and Sakamoto, K. 1998, *ApJ*, 494, 236
- Wada, K., and Norman, C. 2001, *ApJ*, 546, 172

Table 1. Log of observations

Date	Time		H.A.		$t_{\text{middle}}$ (J.D.)	Config.	$t_{\text{cycle}}$ min
	Start	End	Start	End			
1999 Nov 29	18 <sup>h</sup> 58 <sup>m</sup>	25 <sup>h</sup> 10 <sup>m</sup>	−1 <sup>h</sup> 2	5 <sup>h</sup> 0	2451512.42	D	30
1999 Nov 30	17 10	23 25	−2.9	3.3	2451513.35	D	30
1999 Dec 27	17 24	23 25	−0.9	5.1	2451540.35	D	20
2000 Jan 1	17 37	23 25	−0.3	5.4	2451545.35	D	20
2000 Jan 3	16 41	23 25	−1.2	5.6	2451547.34	D	20
2000 Jan 11	13 37	22 55	−3.7	4.4	2451555.26	AB	20
2000 Apr 18	06 45	16 25	−4.1	5.5	2451652.98	D	20
2000 Apr 29	06 06	14 25	−4.1	4.2	2451663.93	D	20
2000 Apr 30	05 28	14 25	−4.6	4.3	2451664.91	D	20

Note. — Observing date and time are in UT. Hour angle of M81 is in hours. In each cycle of duration  $t_{\text{cycle}}$ , gain calibrator is observed for 3 min; 2 min is used to slue telescopes; and M81 is observed for the rest.

Table 2. Flux density of M81\*

$t_0$ (JD)	$\Delta T_{\text{obs}}$ day	$\overline{S_{3\text{mm}}}$ Jy	$(dS_{3\text{mm}}/dt)/S_{3\text{mm}}(t_0)$ day <sup>-1</sup>	$\tau_2$ day
2451512.29	0.26	0.25	$0.62 \pm 0.18$	1.6
2451513.22	0.26	0.40	$1.66 \pm 0.18$	0.6
2451540.22	0.25	0.51	$0.22 \pm 0.18$	4.5
2451545.23	0.24	0.63	$1.91 \pm 0.09$	0.5
2451547.20	0.28	0.98	$-0.32 \pm 0.05$	1.6
2451555.07	0.39	0.35	$-0.71 \pm 0.13$	0.7
2451652.78	0.40	0.25	$0.56 \pm 0.14$	1.8
2451663.75	0.35	0.15	...	...
2451664.73	0.37	0.21	$1.37 \pm 0.19$	0.7

Note. — Observations of M81 start at time  $t_0$  and last for the duration of  $\Delta T_{\text{obs}}$ . Mean flux density of M81\* during observations is  $\overline{S_{3\text{mm}}}$ , with the absolute calibration error of about 10%. Flux densities in each transit are fitted with a linear function,  $S_{3\text{mm}}(t) = S_{3\text{mm}}(t_0) + \frac{dS_{3\text{mm}}}{dt}(t - t_0)$ . Gain correction has been applied before fitting. No fitting was made for the data taken on J.D. = 2451663, because of poor signal-to-noise ratio. The timescale  $\tau_2$  is the time in which the flux density would double or become half if the linear variation held.



Table 3. Key radii in the model

$M_{\text{BH}}$ $M_{\odot}$	$R_{\text{nt}}$ pc	$R_{\text{NILR}}$ pc	$\max(R_{\text{NILR}})$ pc	$R_{\text{IILR}}$ pc
$10^6$	17	28	84	279
$10^7$	37	82	137	284
$10^8$	82	... †	237	...

Note. — Key radii in the simulations shown in Fig. 8. The model potential is eq. (14) and the pattern speed of the bar is  $\Omega_{\text{bar}} = 50 \text{ km s}^{-1} \text{ kpc}^{-1}$ . See text for other parameters in the model.

†The minimum of  $\Omega - \kappa/2$  is  $60 \text{ km s}^{-1} \text{ kpc}^{-1}$  and hence, strictly speaking, an NILR does not exist. However the characteristic gas feature of NILR appears at radii where  $\Omega - \kappa/2 \approx \Omega_{\text{bar}}$ .

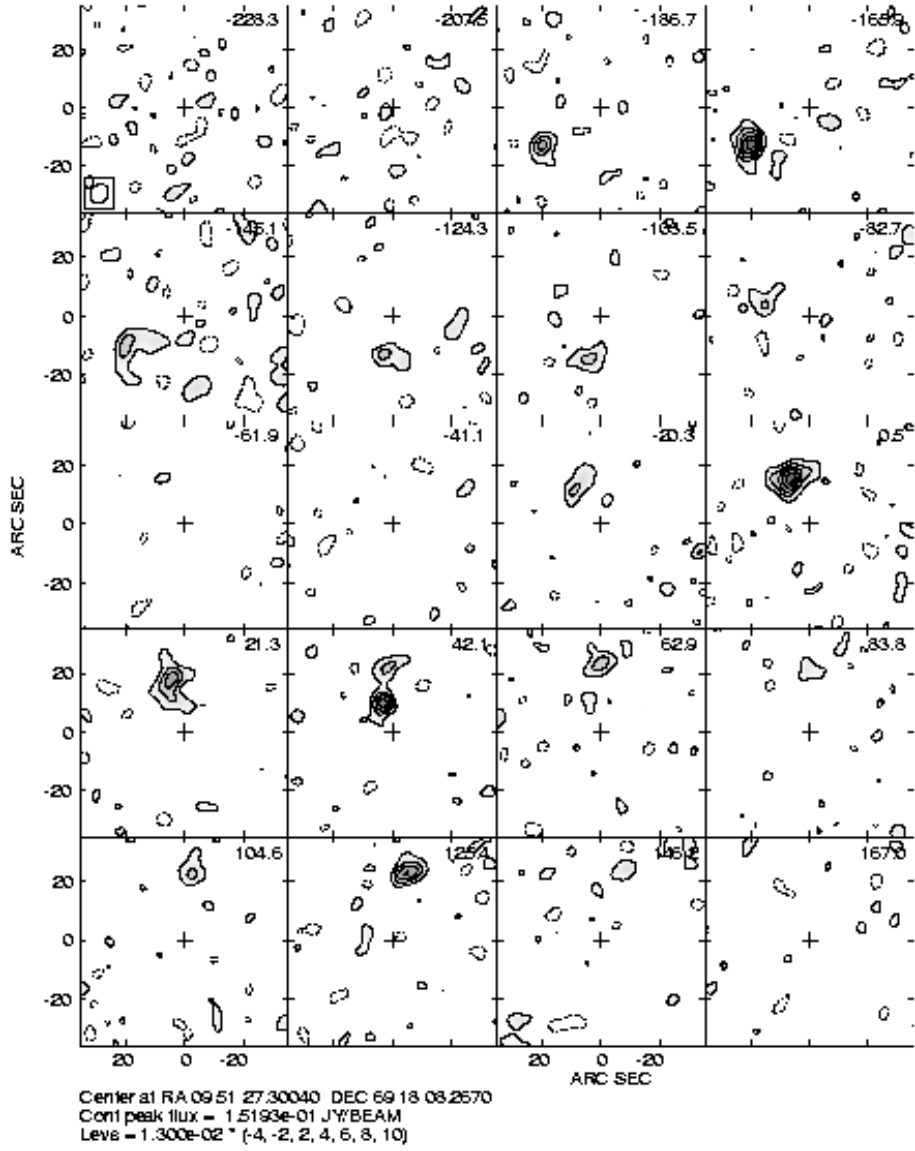


Fig. 1.— CO(J=1-0) channel maps of  $20.8 \text{ km s}^{-1}$  resolution in the central kpc of M81. Continuum emission from the nucleus (shown as a cross) has been subtracted. Contours are at  $-4, -2, 2, 4, 6, 8,$  and  $10 \times 13 \text{ mJy beam}^{-1}$  ( $= 30 \text{ mK} = 1\sigma$ ). LSR velocity ( $\text{km s}^{-1}$ ) is shown in each panel. The synthesized beam of  $6''.9 \times 5''.8$  in FWHM is shown in the bottom left corner of the first panel.

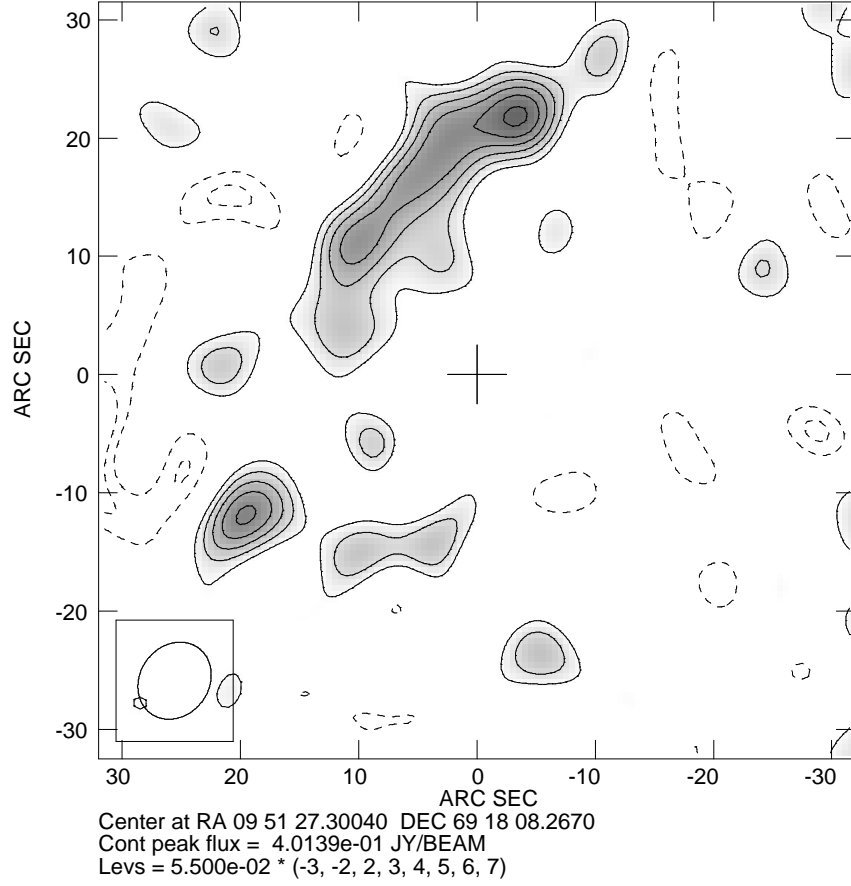


Fig. 2.— Integrated intensity map of CO(J=1–0) emission in the central kpc of M81. Continuum emission from the nucleus at the position of the cross has been subtracted. Contours are at  $-3, -2, 2, 3, 4, 5, 6,$  and  $7 \times 1.1 \text{ Jy beam}^{-1} \text{ km s}^{-1}$  ( $= 1\sigma$ ). The contour interval and peak integrated intensity correspond to molecular gas column density of  $17$  and  $120 M_{\odot} \text{ pc}^{-2}$ , respectively. The synthesized beam of  $6''.9 \times 5''.8$  in FWHM is shown in the bottom left corner.

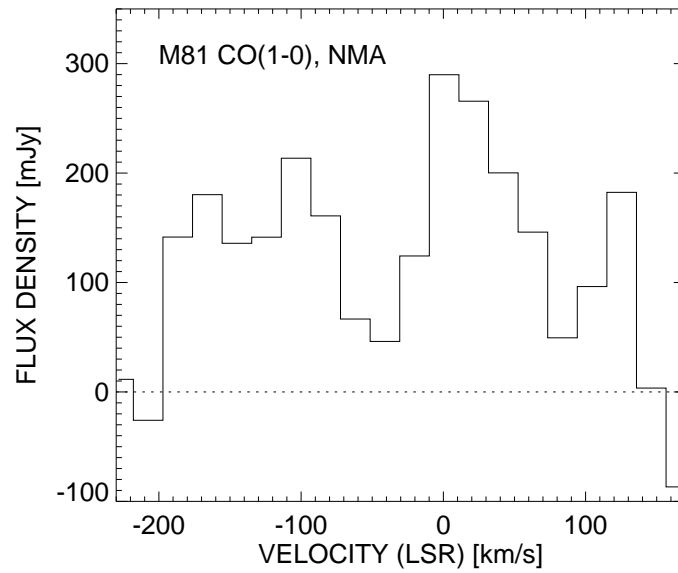


Fig. 3.— Spectrum of CO(J=1–0) emission in the central kpc of M81, observed in the 1′ (FWHM) primary beam of the NMA. The line width is  $\sim 350 \text{ km s}^{-1}$  and the detected CO flux is  $50 \text{ Jy km s}^{-1}$ , which is about half of the single-dish flux observed at the NRAO 12 m telescope. Continuum emission from the nucleus has been subtracted.

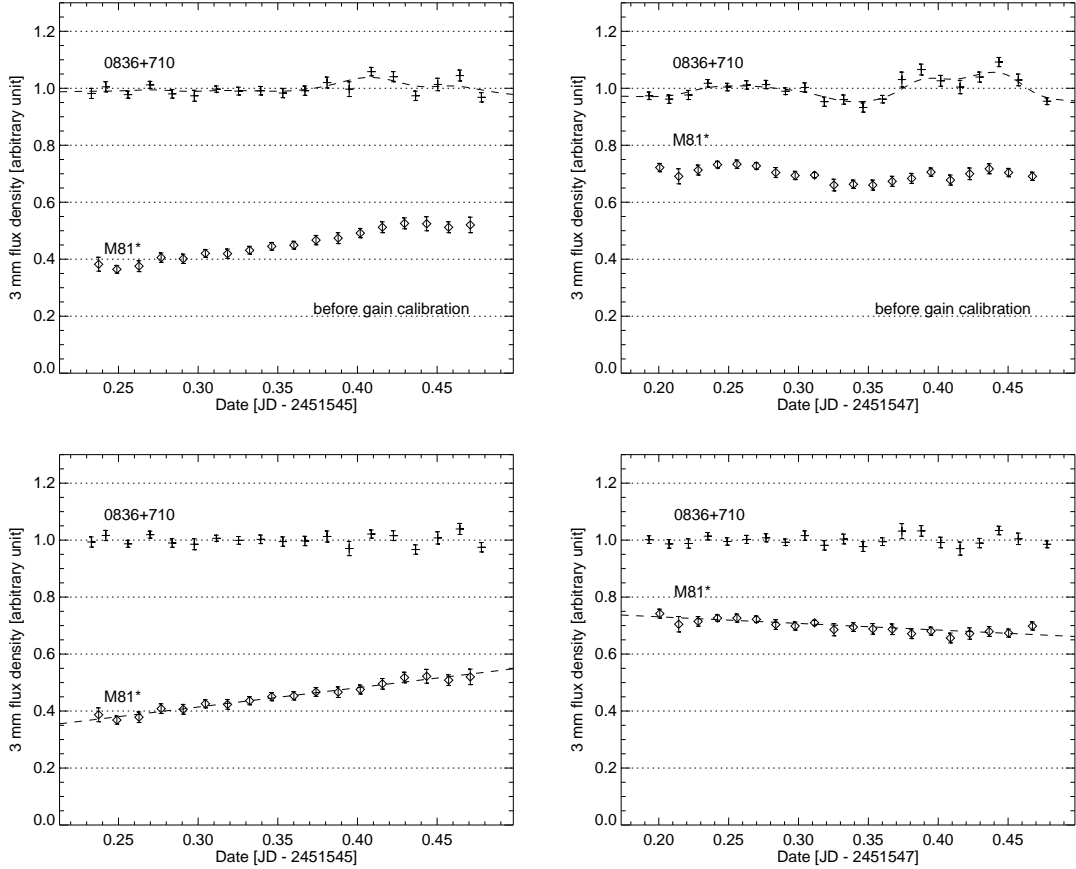


Fig. 4.— Time variation of the 3 mm continuum from M81\* on J.D. = 2451545 (left) and 2451547 (right). Top panels show data after chopper-wheel correction and before gain calibration. Gain curves (shown as dotted lines) are derived by smoothing amplitudes of B0836+710 with a Gaussian kernel having  $\sigma = 0.015$  day and a cutoff at  $|\Delta t| = 0.050$  day. The large gain variation in the right panel, on J.D. = 2451547, is most likely due to coherence loss. Bottom panels show data after applying the gain calibration. A linear fit of M81\* is plotted over the calibrated data. The monotonic variation of M81\* is clearly seen. Error bars are  $\pm 1\sigma$  for 0836+710 and  $\pm 2\sigma$  for M81\*.

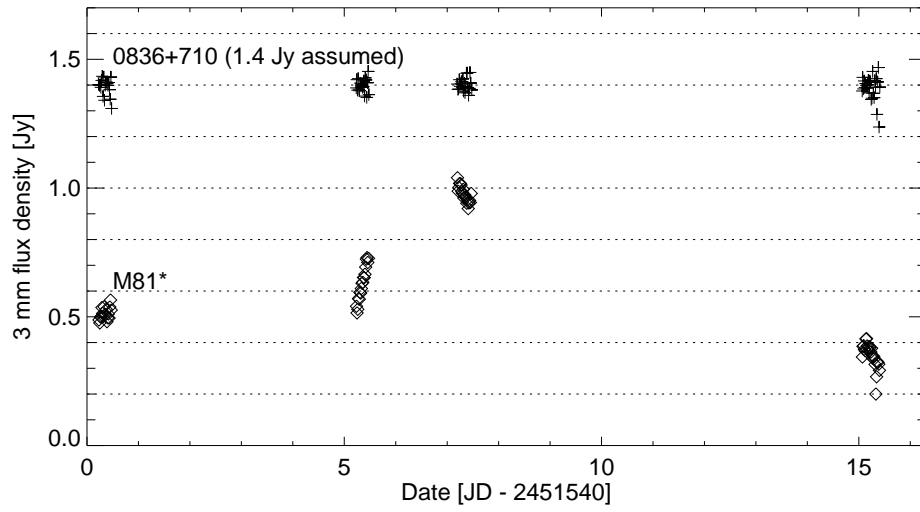


Fig. 5.— Time variation of the 3 mm continuum from M81\* around the flare on J.D.  $\sim 2451546$ . Instrumental gain has been calibrated assuming that 0836+710 had a constant flux density of 1.4 Jy and was unpolarized.

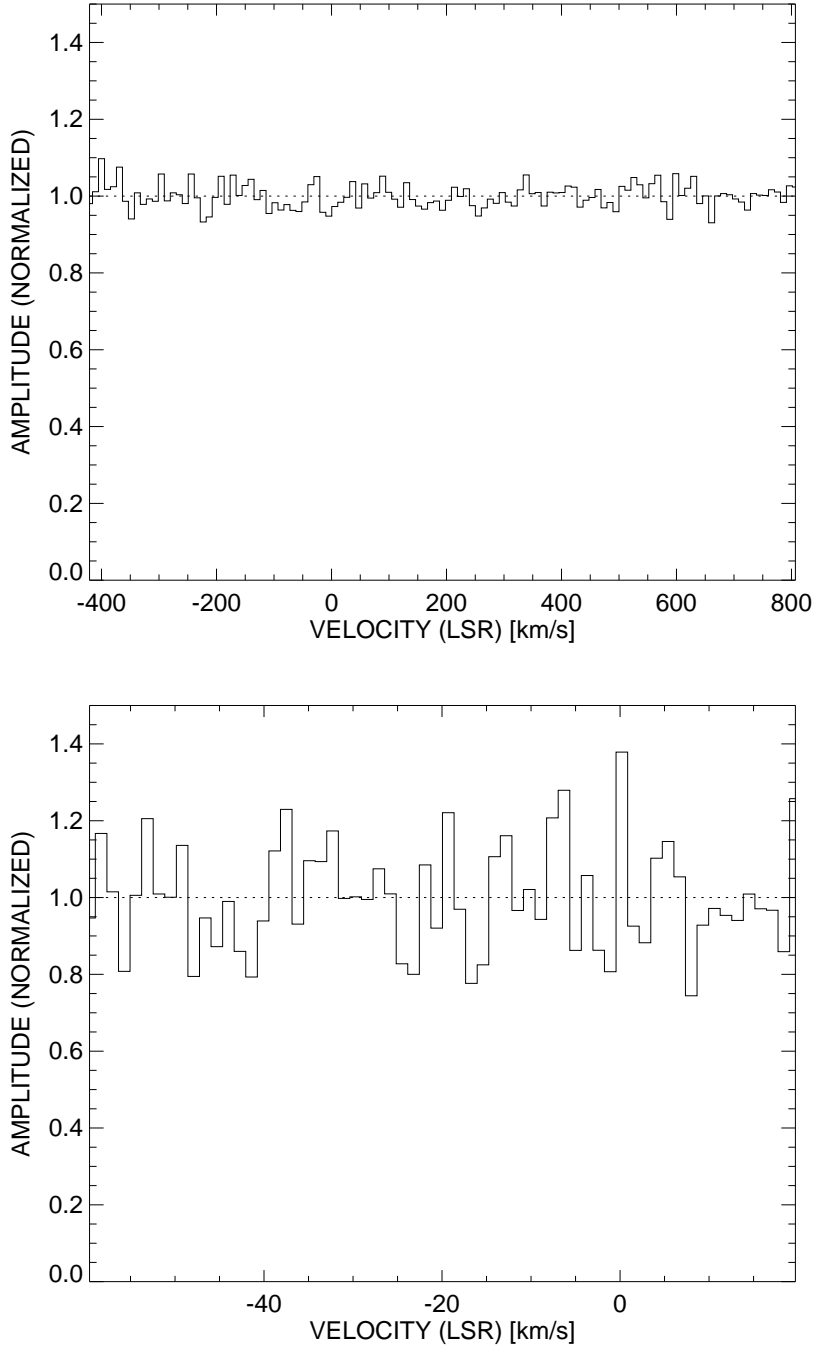


Fig. 6.— Spectra of the 3 mm continuum from M81\* used to search for CO(J=0–1) absorption toward the nucleus. The top panel has a 10.4 km s<sup>-1</sup> resolution (obtained from UWBC), while the bottom panel has a 1.3 km s<sup>-1</sup> resolution (observed with FX). A linear baseline is subtracted and amplitude is normalized to unity. The systemic velocity of M81 is  $-34$  km s<sup>-1</sup> (LSR) and Galactic HI clouds have velocities around 3 km s<sup>-1</sup> (LSR) in the direction of M81. No absorption is seen around these velocities. The rms of the UWBC spectrum is 0.0315 and that of the FX spectrum is 0.140.

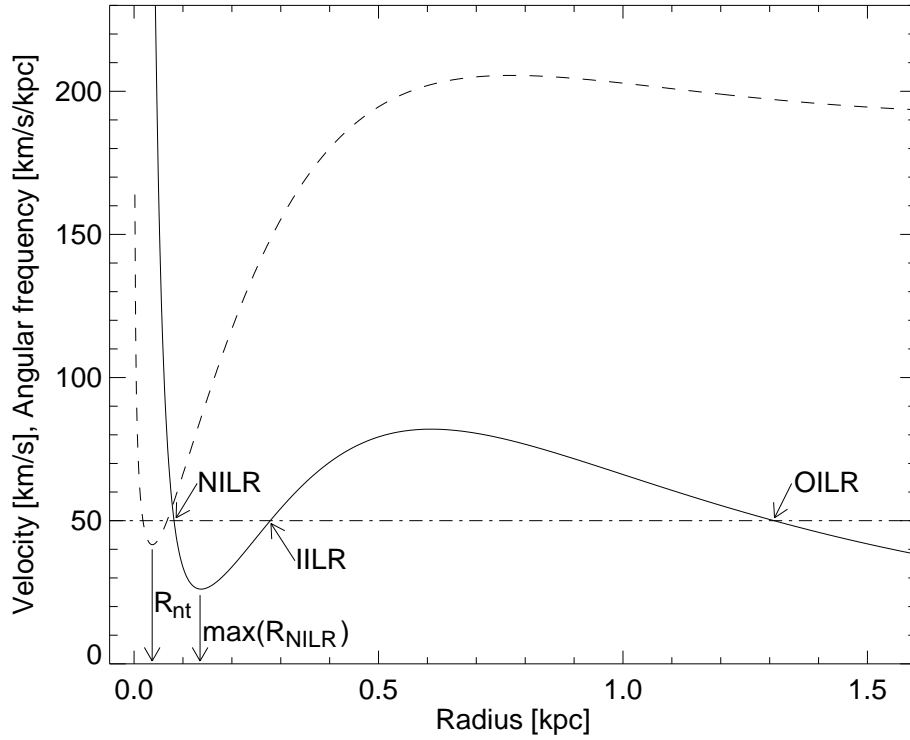


Fig. 7.— The rotation curve (dashed line) and  $\Omega - \kappa/2$  curve (solid line) for a model potential with a  $10^7 M_\odot$  black hole at the galactic center. The minimum of the rotation curve at  $R_{nt}$  and the minimum of  $\Omega - \kappa/2$  at  $R = \max(R_{NILR})$  are indicated. Also marked are the nuclear inner Lindblad resonance (NILR), inner inner Lindblad resonance (IILR), and outer inner Lindblad resonance (OILR) for a bar pattern speed of  $50 \text{ km s}^{-1} \text{ kpc}^{-1}$  (dot-dashed line).



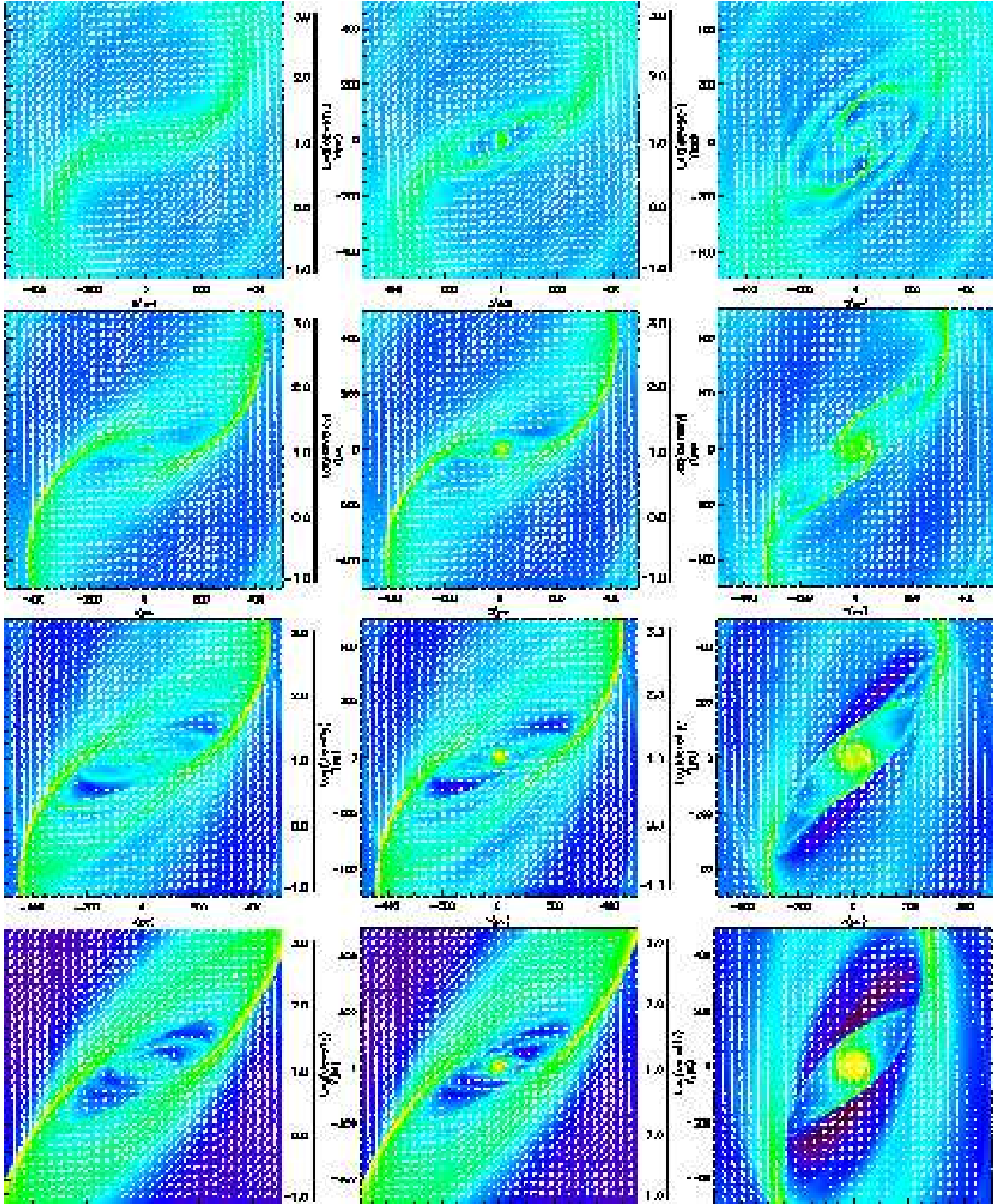


Fig. 8.— Simulations of gas dynamics in the galactic center with a massive black hole and bar perturbations. Each panel shows gas surface density in pseudocolor, and gas velocities with arrows, in the frame rotating with the bar. The major axis of the bar is horizontal and the rotation of the galaxy is counterclockwise. The three columns are, from right to left, for the mass of the central black hole of  $10^6$ ,  $10^7$ , and  $10^8 M_{\odot}$  respectively. The four rows are, from the top, at  $T = 20$ ,  $40$ ,  $60$ , and  $86$  Myr. The orbital period of the system at the radius of  $500$  pc is  $15$  Myr.